



HAL
open science

Multiparametric quantification of the heterogeneity of free Ca^{2+} concentration by ^{19}F MR spectroscopy

Norbert W Lutz, Monique Bernard

► **To cite this version:**

Norbert W Lutz, Monique Bernard. Multiparametric quantification of the heterogeneity of free Ca^{2+} concentration by ^{19}F MR spectroscopy. *Journal of Magnetic Resonance*, 2018, 297, pp.96-107. 10.1016/j.jmr.2018.10.009 . hal-03527732

HAL Id: hal-03527732

<https://hal.science/hal-03527732>

Submitted on 27 Jan 2022

HAL is a multi-disciplinary open access archive for the deposit and dissemination of scientific research documents, whether they are published or not. The documents may come from teaching and research institutions in France or abroad, or from public or private research centers.

L'archive ouverte pluridisciplinaire **HAL**, est destinée au dépôt et à la diffusion de documents scientifiques de niveau recherche, publiés ou non, émanant des établissements d'enseignement et de recherche français ou étrangers, des laboratoires publics ou privés.

21 **Abstract**

22 For biological tissue that is heterogeneous with respect to free intracellular Ca^{2+} concentration ($[\text{Ca}^{2+}]_i$), the
23 lineshape of the ^{19}F MRS resonance of injected $[\text{Ca}^{2+}]$ -sensitive 4-FBAPTA or BAPTA-FF reflects the
24 statistical distribution of $[\text{Ca}^{2+}]_i$ values. While conventional ^{19}F MRS of these fluorinated Ca^{2+} reporter
25 molecules only provides one $[\text{Ca}^{2+}]_i$ value per spectrum, our specially designed lineshape analysis reveals
26 at least eight quantitative statistical parameters (descriptors) characterizing the $[\text{Ca}^{2+}]_i$ distribution within
27 the observed tissue volume. To this end, the $[\text{Ca}^{2+}]$ -sensitive ^{19}F MRS resonance is transformed into a
28 $[\text{Ca}^{2+}]_i$ curve. Subsequently, the digital points of this $[\text{Ca}^{2+}]_i$ profile are used to build a histogram using
29 dedicated algorithms. The following statistical descriptors are computed from this histogram: weighted
30 mean and median, standard deviation, range, mode(s), kurtosis, skewness, and entropy. Our new method is
31 thoroughly validated through *in-silico* and experimental models. The potential of combining statistical
32 $[\text{Ca}^{2+}]$ information with spatial resolution is demonstrated by simulated statistical CSI maps. This proof of
33 principle should form the basis of future *in-vivo* studies in physiology and medicine, notably in heart and
34 muscle research.

35

36 **Keywords:** calcium quantitation, tissue heterogeneity, ^{19}F MRS, lineshape analysis, heterogeneity
37 descriptors, statistical distributions, histograms, free intracellular Ca^{2+}

38

39 **Graphical abstract**

40

41 **1. Introduction**

42 Metal ions play fundamental roles in biological organisms. Calcium (Ca^{2+}) is an important second
43 messenger in signal transduction, and is involved in neurotransmitter release from neurons and in muscle

44 contraction [1]. Ca^{2+} is also required as a cofactor by many enzymes. While bone is the principal mineral
45 storage site for calcium, organelles such as mitochondria and the endoplasmic reticulum provide
46 intracellular calcium storage [2]. From these organelles, Ca^{2+} is released during particular cellular events.
47 Thus, the resting Ca^{2+} concentration in the cytosol is only on the order of several 100 nmol, but specific
48 signals can trigger an increase by at least two orders of magnitude. Ca^{2+} is actively pumped from the
49 intracellular to the extracellular space to maintain a $[\text{Ca}^{2+}]$ gradient of a factor of 20,000 to 100,000, as the
50 extracellular Ca^{2+} concentration may easily be in the millimolar range. There is growing evidence that
51 calcium/sodium exchange has particular pathophysiological implications, notably in neurological diseases
52 [3]. Furthermore, calcium metabolism disorders have been associated with gut, kidney and bone [4].

53 The mechanisms behind these disorders are complex, but are critically dependent on the intracellular
54 presence of free Ca^{2+} . Therefore, methods for *in-vivo* measurement of free- Ca^{2+} concentrations in
55 biological tissue have been proposed, *e.g.*, ^{19}F MR spectroscopy (^{19}F MRS) of fluorinated intracellular Ca^{2+}
56 reporters such as 4F-BAPTA (4,4'-difluoro-BAPTA) or 5F-BAPTA (5,5'-difluoro-BAPTA) (5,6). [In the
57 remainder of this work, " Ca^{2+} " exclusively refers to free Ca^{2+} , unless specified otherwise]. Although both
58 4F-BAPTA and 5F-BAPTA specifically form chelates with Ca^{2+} , 4F-BAPTA is characterized by fast
59 exchange (on the NMR time scale) with Ca^{2+} , but 5F-BAPTA by slow exchange. These chelators were
60 employed to determine intracellular $[\text{Ca}^{2+}]$ in thymocytes from BALB/c mice [5,6], in pig lymphocytes,
61 Ehrlich ascites tumor cells, rat basophil leukemic cells and perfused rat hearts [6], but also in intact ferret
62 hearts (notably by Marban et al. [7,8]), and in rabbit hearts [9]. Another fast-exchange Ca^{2+} chelator,
63 BAPTA-FF (5,5',6,6'-tetrafluoro-BAPTA), has also been used to study intracellular free Ca^{2+} in rabbit and
64 rat heart by ^{19}F MRS [10–12]. Note that all cardiac experiments mentioned here have been done
65 successfully on the beating heart. Unsurprisingly, applications *in vivo* and *in situ* soon followed, *e.g.*,
66 intracellular $[\text{Ca}^{2+}]$ measurements in kidney, spleen, and brain of male Sprague-Dawley rats by using ^{19}F
67 MRS of 5F-BAPTA [13]. Thus, feasibility and sufficient sensitivity of the F-BAPTA ^{19}F MR spectroscopic
68 technique in general has been unequivocally proven for intact, living mammals.

69

70

71 Newer developments were directed at yielding information on spatial Ca^{2+} distribution within the studied
72 organ or tissue region. For instance, ^{19}F CEST MRI of 5F-BAPTA has been suggested for mapping Ca^{2+}
73 concentration [14], benefiting from signal amplification through saturation transfer. Alternatively,
74 Angelovski et al. have developed a range of smart Ca^{2+} -sensitive T_1 relaxation agents designed to enable
75 (mostly extracellular) Ca^{2+} imaging based on the water ^1H signal [15,16]. While these recently presented
76 methods are expected to provide some information on the physical location of tissue regions characterized
77 by differing Ca^{2+} concentrations, they only partially reflect the $[\text{Ca}^{2+}]$ variations actually existing within
78 the object studied. This intrinsic shortcoming is due to the fact that methods based on digital images only
79 yield one single concentration value for each image pixel, the latter representing a voxel from within the
80 imaged object. Thus, any heterogeneity with respect to Ca^{2+} concentration within such a voxel is
81 necessarily ignored, and is replaced by a single concentration value that may or may not be close to the
82 average value for that voxel. The relatively large voxel sizes typically used in such mapping techniques
83 (several microliters) aggravate the problem, as tissue voxels of this order of magnitude are biologically
84 heterogeneous and comprise different microenvironments.

85 We suggest here a new approach taking into account the entire (microscopic as well as macroscopic)
86 heterogeneity of tissue with respect to intracellular Ca^{2+} concentrations. Our concept is based on the
87 paradigm that the overall line shape of an MRS resonance whose chemical shift is a function of Ca^{2+}
88 concentration, directly reflects the statistical distribution of the Ca^{2+} concentrations within the probed
89 tissue volume. For $[\text{Ca}^{2+}]$ analysis by ^{19}F MRS of fluorinated chelators, this implies that fast exchange
90 between metal ion and ligand is required. At present, our algorithms provide at least eight quantitative
91 statistical descriptors (in addition to one or several modes, *i.e.*, maxima of the distribution curve)
92 characterizing the distribution of Ca^{2+} concentration values: mean, median, standard deviation, range,
93 skewness (asymmetry), kurtosis (pointedness), standard and normalized entropy (smoothness). In many

92 cases, the relative sizes of sample regions representing characteristic concentration ranges may also be
93 calculated. The underlying formal scheme is similar to the algorithms previously introduced by us to
94 analyze heterogeneity in Mg^{2+} concentration [17], pH [18] and temperature [19,20] by ^{31}P or ^1H MRS,
95 respectively; these papers [17–20] discuss mathematical details of general importance to the quantification
96 of the heterogeneity of physicochemical parameters by way of statistical MRS line shape analysis.

97 In addition to presenting our algorithm, we provide the proof of principle by transforming experimental
98 BAPTA-FF ^{19}F MR spectral lines into statistical distribution curves for Ca^{2+} concentrations, *i.e.*, into the
99 corresponding statistical concentration profiles. Although both BAPTA-FF and 4F-BAPTA form fast
100 exchanging complexes with Ca^{2+} , 4F-BAPTA is not currently commercially available. Nonetheless, we
101 assess the potential of 4F-BAPTA by numerically modeling ^{19}F MR spectra as a function of Ca^{2+}
102 concentration. These are not *ab-initio*, but empirical simulations; both chemical shift and linewidth values
103 are taken from actual ^{19}F MR spectroscopy experiments previously conducted on 4F-BAPTA solutions in
104 the presence of varying Ca^{2+} concentrations [5,21], at a time when 4F-BAPTA was still available
105 commercially. This bestows high practical relevance upon our calculated models.

106 The mathematical and statistical equations given here are formally analogous to the equations presented
107 previously for studying Mg^{2+} concentrations [17]. Therefore, the basic mathematical validity of the
108 transformation of MR line shapes to ion concentration profiles, and the justification for deriving statistical
109 parameters from these profiles, are already documented [17], and will not be repeated here. The purpose of
110 our current validation is to examine the following questions: (i) How do the resulting quantitative
111 descriptors of statistical $[\text{Ca}^{2+}]$ distribution have to be interpreted in terms of distribution curve properties?
112 (ii) What are the ranges of the statistical descriptor values for $[\text{Ca}^{2+}]$ distribution curves to be expected
113 from actual *in-vivo* experiments? (iii) How sensitive are the resulting $[\text{Ca}^{2+}]$ distribution curves, and their
114 associated descriptor values, to actual $[\text{Ca}^{2+}]$ gradients *vs.* spurious effects, *i.e.*, curve shape contributions
115 unrelated to $[\text{Ca}^{2+}]$ distribution? (iv) What are the effects of ^{19}F MR line shape correction by our empirical

116 deconvolution method on the resulting distribution curve shapes and, consequently, on the derived
117 descriptors of $[Ca^{2+}]$ concentration profiles?

118 Moreover, we discuss potential and limitations of our method. Based on our results, we also suggest the
119 development of further $[Ca^{2+}]$ reporter molecules optimized for use in our analysis of statistical
120 distributions. When used with monovoxel ^{19}F MR acquisition, our analysis is fast and will provide
121 valuable statistical information that is complementary to the spatially resolved data obtainable by the Ca^{2+}
122 mapping techniques mentioned above. When used in multivoxel ^{19}F MR experiments such as chemical-
123 shift imaging (CSI), our new method will be able to generate a combination of full statistical and some
124 spatial information on the distribution of these metal ion concentrations in one single experiment; this is
125 demonstrated by parameterized CSI maps modeled with calculated $[Ca^{2+}]$ profiles. Once translated to the
126 field of biomedical research, our multiparametric analysis is expected to significantly enhance the analysis
127 of intracellular free Ca^{2+} concentrations *in vivo* by offering detailed quantitative characterization of tissue
128 heterogeneity with respect to $[Ca^{2+}]$, thus complementing fast $[Ca^{2+}]$ mapping by ^{19}F -CEST or other MRI
129 methods. We also briefly discuss the potential of our approach in the context of the increasingly important
130 data analysis by "machine learning" procedures.

131

132 **2. Theory**

133 The use of ^{19}F MRS for measuring Ca^{2+} concentrations is based on the dependence of the chemical shift,
134 δ , of a ^{19}F resonance of the reporter molecule (ligand) in question (4F/4'F of 4F-BAPTA, or 5F/5'F of
135 BAPTA-FF), on the concentration of free Ca^{2+} to be determined. The relationship between the measured
136 chemical shift, δ_{mea} , and $[Ca^{2+}]$ is given by the following general equations [22], in strict analogy with
137 equations previously used for $[Mg^{2+}]$ [17]:

138

eq.1

139 with
$$\Phi = \frac{[BAP]_f}{[BAP]_{tot}} = \frac{\delta_{mea} - \delta_{CaBAP}}{\delta_{BAP} - \delta_{CaBAP}} \quad \text{eq.2}$$

140 with K_d^{CaBAP} , dissociation constant of complex between Ca^{2+} and BAP (BAP = BAPTA-FF or 4F-
141 BAPTA); $[BAP]_f$, concentration of free (uncomplexed) BAP; $[BAP]_{tot}$, total concentration of BAP (= sum
142 of free and Ca^{2+} -complexed [BAP]); δ_{BAP} , ^{19}F chemical shift for free (uncomplexed) BAP; δ_{CaBAP} , Ca^{2+} -
143 sensitive ^{19}F chemical shift for BAP complexed with Ca^{2+} . K_d^{CaBAP} , δ_{BAP} and δ_{CaBAP} have been determined
144 experimentally. Their actual values in different biological tissues may vary slightly as a function of
145 intracellular parameters such as pH and ionic strength; thus, appropriate calibration is necessary for
146 accurate results, notably for biological applications. K_d^{CaBAP} values are obtainable from the published
147 literature, as well as the δ_{BAP} and δ_{CaBAP} values for 4F-BAPTA [21,23]. Note that K_d^{CaBAP} is substantially
148 larger for BAPTA-FF (65 μM) than for 4F-BAPTA (2.9 μM). This makes BAPTA-FF particularly useful
149 in cases where $[Ca^{2+}]$ values lie substantially above basal levels characteristic of most cells, while 4F-
150 BAPTA is appropriate for $[Ca^{2+}]$ values closer to basal levels; further advantages of BAPTA-FF have been
151 described elsewhere [23]. For 5F/5'F of BAPTA-FF, δ_{BAP} and δ_{CaBAP} values are confirmed experimentally.
152 Special calibration techniques may also take into account pH and other effects on the ^{19}F MRS resonances
153 of the reporter molecules, depending on tissue type and physiological conditions. However, since our
154 current report is strictly focused on the proof of principle of our statistical approach, we do not currently
155 include fine-tuning through tissue-specific chemical shift-to- $[Ca^{2+}]$ conversion algorithms. A practical
156 example of our calculations is presented in the template provided as an EXCEL spreadsheet in
157 Supplementary Information (S1 Supplemental Software). Further explanations pertaining to the general
158 paradigm underlying our method, as well as to the statistical parameters that can be determined, are
159 contained in Supplementary Information (S1 Supplemental Materials).

160

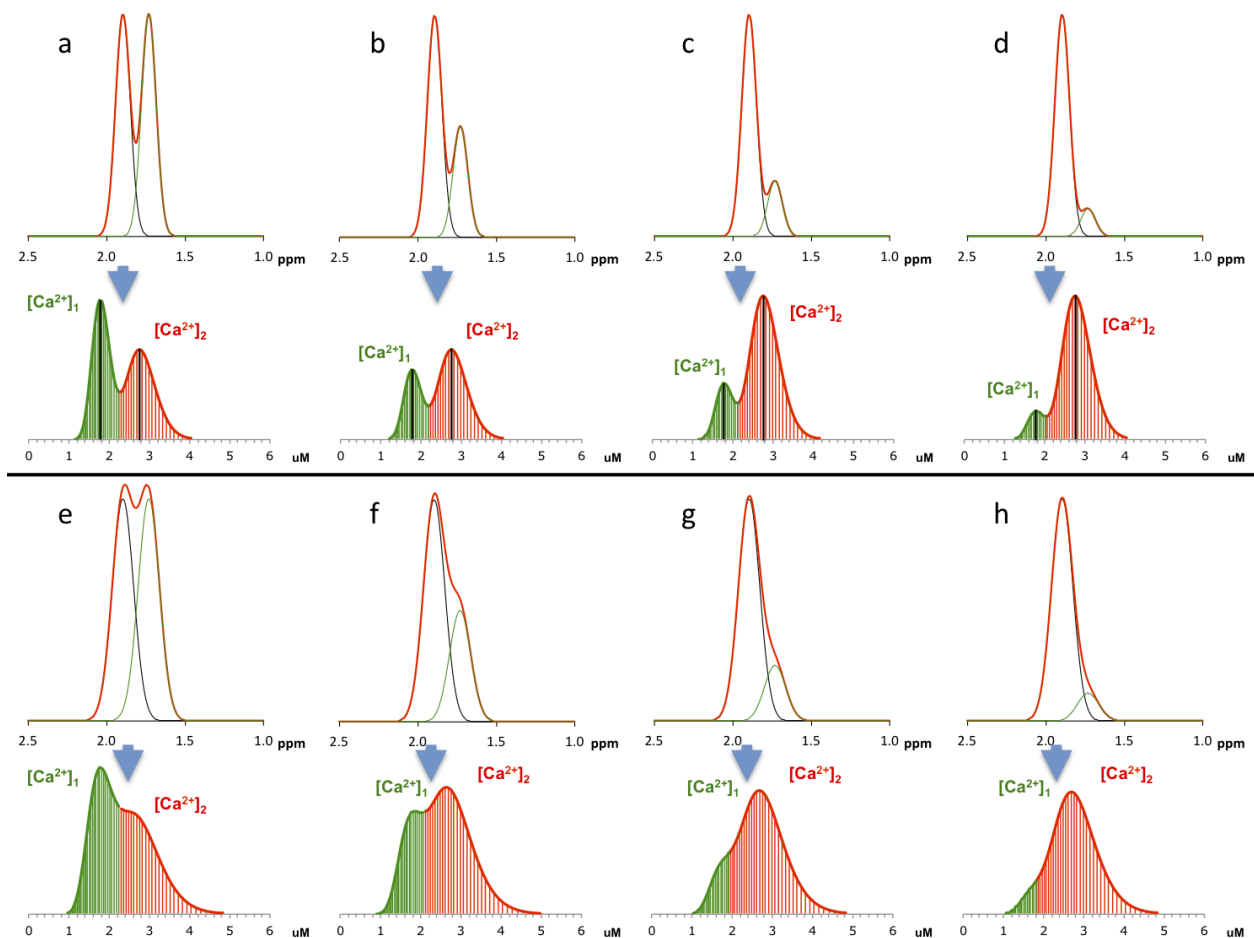
161 3. Results

162 **3.1. Studies of multimodal $[Ca^{2+}]$ profiles - overview.** Most tissues containing cells that exhibit a range
163 of different Ca^{2+} concentrations are likely characterized by complex $[Ca^{2+}]$ distributions due to genetic,
164 physiological, metabolic and other growth conditions varying throughout the studied tissue volume. The
165 presence of heterogeneous cell populations may also contribute to a lack of $[Ca^{2+}]$ homogeneity [24].
166 However, for the purpose of validating our method we initially focused on numerically simulated and
167 experimental unimodal and bimodal $[Ca^{2+}]$ profiles, because the concept of quantitative parameters of
168 $[Ca^{2+}]$ heterogeneity is best tested on the basis of well-defined distribution functions. For $[Ca^{2+}]$
169 investigations with BAPTA-FF as reporter molecule, experimental $[Ca^{2+}]$ distribution models were
170 generated, based on specially designed samples (phantoms). By contrast, we had to limit our
171 Ca^{2+} /4-FBAPTA studies to numerical simulations because 4-FBAPTA is not currently available as a
172 commercial product, as indicated in the Introduction section. Our simulations were performed for field
173 strengths of 4.7 T and 7.0 T. These values were chosen based on the following considerations. First, we
174 see a significant potential for our method primarily in preclinical research; this lead us to not focus on
175 field strengths more common for clinical instruments, such as 3 T. On the other hand, focusing on very
176 high fields would be problematic for currently existing fluorinated Ca^{2+} reporter molecules because at very
177 high fields, the exchange between Ca^{2+} and chelator may no longer be in the fast-exchange range on the
178 NMR scale (e.g., for Ca^{2+} /BAPTA-FF there is a borderline situation of "fast-intermediate" exchange
179 already starting from 8.5 T [23]). Our evaluations are in keeping with our previous validations for $[Mg^{2+}]$
180 distributions [17]. As in the latter case, most quantitative parameters suggested in this report are
181 universally applicable to any given distribution of concentration values. Taken together, the parameter
182 values given in our tables and diagrams explore the basic behavior to be expected for statistical descriptors
183 in *in-vivo* distribution curves.

184

185

186



187 **Figure 1.** Simulated 4FBAPTA ^{19}F MRS resonances and their envelopes (first and third row), and $[\text{Ca}^{2+}]$
 188 profiles derived from the respective envelopes (second and fourth row). The spectral envelopes represent
 189 the sums of two partially overlapping Gaussians, for amplitude ratios (upfield : downfield) 1:1 (a,e), 1:2
 190 (b,f), 1:4 (c,g) and 1:8 (d,h). The centers of the individual Gaussians underlying each envelope were
 191 chosen to be at 1.73 and 1.90 ppm in all cases; the linewidth of each individual Gaussian was 30 Hz,
 192 corresponding to 0.11 ppm at 7.0 T (a - d), and 0.16 ppm at 4.7 T (e - h). Areas that can be associated with
 193 distinct modes are color-coded. The vertical black lines represent $[\text{Ca}^{2+}]$ distributions in the form of Dirac
 194 δ functions. The right tails of the $[\text{Ca}^{2+}]$ distributions (second and fourth row) decrease more slowly to the
 195 baseline than the left tails. The origin of this asymmetry, introduced by ppm-to- $[\text{Ca}^{2+}]$ conversion, is the
 196 nonlinearity between the ppm and the $[\text{Ca}^{2+}]$ scales, as mentioned in the text. This nonlinearity "stretches"
 197 the distribution curve out to the right, and "compresses" it to the left for the particular concentration ranges
 198 chosen. A well visible consequence of these effects is the difference in line width; the " $[\text{Ca}^{2+}]_2$ " widths are
 199 larger than the " $[\text{Ca}^{2+}]_1$ " widths, although in the underlying simulated spectra (first and third row), both
 200 simulated resonances have identical widths.

201

202 **Table 1.** Statistical descriptors for $[Ca^{2+}]$ curves based on *in-silico* models of Gaussian ^{19}F MR resonances
203 of 4F-BAPTA

204

descriptors for 7 T	1:1 ^a	1:2 ^b	1:4 ^c	1:8 ^d
weighted mean (μM)	2.32	2.49	2.62	2.72
weighted median (μM)	2.25	2.58	2.69	2.75
std. deviation (μM)	0.59	0.58	0.53	0.47
range (μM)	3.18	3.21	3.18	3.17
mode, mg_1 (μM)	1.77	1.77	1.77	1.77
mode, mg_2 (μM)	2.76	2.76	2.76	2.76
global max. (μM)	1.77	2.76	2.76	2.76
peak height ratio ($h_1:h_2$)	1.55	0.78	0.39	0.20
peak area ratio integ. ($a_1:a_2$)	0.99	0.49	0.24	0.11
skewness, G1	0.343	-0.051	-0.314	-0.362
kurtosis, G2	-0.906	-0.831	-0.295	0.364
stand. entropy, H_s	3.15	3.08	2.91	2.72
norm. entropy, H_n	0.5559	0.5486	0.5126	0.4864

205

206

207

208

209

210

211

212

descriptors for 4.7 T	1:1 ^e	1:2 ^f	1:4 ^g	1:8 ^h
weighted mean (μM)	2.34	2.51	2.65	2.74
weighted median (μM)	2.25	2.50	2.65	2.72
std. deviation (μM)	0.68	0.68	0.65	0.61
range (μM)	4.18	4.63	4.12	4.12
mode, mg_1 (μM)	1.77	1.86	1.77	1.67
mode, mg_2 (μM)	2.62	2.62	2.69	2.69
global max. (μM)	1.77	2.62	2.69	2.69
peak height ratio ($h_1:h_2$)	1.45	0.81	0.44	0.22
peak area ratio integ. ($a_1:a_2$)	1.04	0.43	0.17	0.07
skewness, G1	0.595	0.350	0.214	0.235
kurtosis, G2	-0.083	-0.142	0.007	0.288
stand. entropy, H_s	3.45	3.40	3.26	3.12
norm. entropy, H_n	0.5798	0.5587	0.5527	0.5287

213

214 Indices a - h refer to diagrams shown in Fig. 1

215

216 **3.2. Validation of statistical algorithms by way of simulated bimodal $[\text{Ca}^{2+}]$ profiles corresponding to**

217 **4-FBAPTA ^{19}F MRS resonances.** First, effects of varying $[\text{Ca}^{2+}]$ heterogeneity on $[\text{Ca}^{2+}]$ distribution

218 parameters were studied for $[\text{Ca}^{2+}]$ profiles derived from the envelopes of two simulated, partially

219 overlapping Gaussian (Fig. 1) or Lorentzian (Fig. S1) 4-FBAPTA ^{19}F resonances centered at 1.73 and 1.90

220 ppm (30 Hz linewidth). Note that spectral envelopes change in shape when converted to $[\text{Ca}^{2+}]$ profiles,

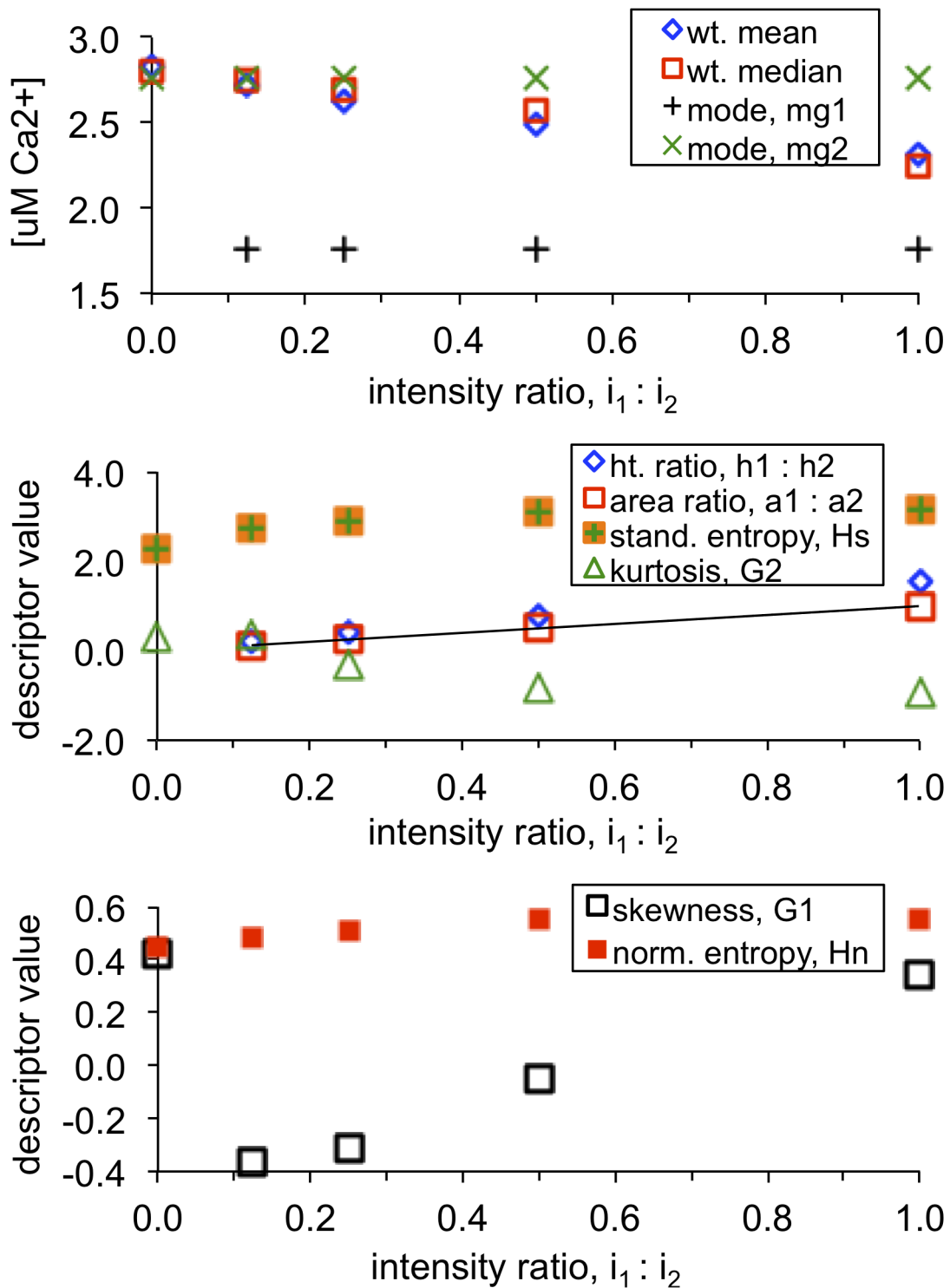
221 due to the nonlinear relationship between chemical shift and $[\text{Ca}^{2+}]$. As the relative amplitudes of the

222 resonances (upfield : downfield ratios) decrease from left to right (Fig. 1, first and third row), the

223 respective derived $[\text{Ca}^{2+}]$ profiles change shapes correspondingly (Fig. 1, second and fourth row), with

224 $[\text{Ca}^{2+}]_2$ modes increasingly dominating associated $[\text{Ca}^{2+}]_1$ modes. The two modes differing by 1.0 μM can
225 be much better discerned for 7.0-T simulations (second row) than for 4.7-T simulations (fourth row).

226 While inspection of Figure 1 allows one to qualitatively assess the distinctness of adjacent modes,
227 quantitative evaluation is made possible by comparing statistical descriptor values as a function of mode
228 intensity ratios. In Figure 2, select descriptor values are plotted against intensity ratios for rapid
229 identification of dominating trends. Since the changes in some descriptor values are rather subtle, we also
230 provide the complete set of numerical data in Table 1 that additionally includes results for 4.7-T
231 simulations. The improved distinction of two modes differing by 1.0 μM for 7.0-T vs. 4.7-T simulations
232 mentioned at the end of the preceding paragraph, is reflected in larger high-field changes (with resonance
233 amplitudes) for those descriptors that characterize profile shapes, *i.e.*, skewness, kurtosis, standard and
234 normalized entropy (Table 1). For instance, normalized entropy, H_n , decreases only by about 0.05 units for
235 the low-field profiles, but by about 0.07 units for the high-field profiles when going from the nearly
236 symmetric distribution (height ratio 1:1) to increasingly asymmetric distributions (down to 1:8). In
237 addition, skewness varies by no more than 0.4 units for the low-field profiles, but by 0.7 units for the high-
238 field profiles. The same trends hold for max. kurtosis increase (by 0.37 and 1.26, respectively), and for
239 max. standard entropy decrease (by 0.33 and 0.47, respectively).



241 **Figure 2.** Statistical descriptors for the [Ca²⁺] profiles presented in Figure 1 a - d, and for a [Ca²⁺] profile
 242 obtained from a unimodal simulated Gaussian resonance ($i_1:i_2 = 0$). The straight line in the center panel

243 shows that mode area ratios, $a_1:a_2$, are proportional to intensity ratios, $i_1:i_2$. Note that the units of the
244 parameters shown in the middle and bottom panels are dimensionless.

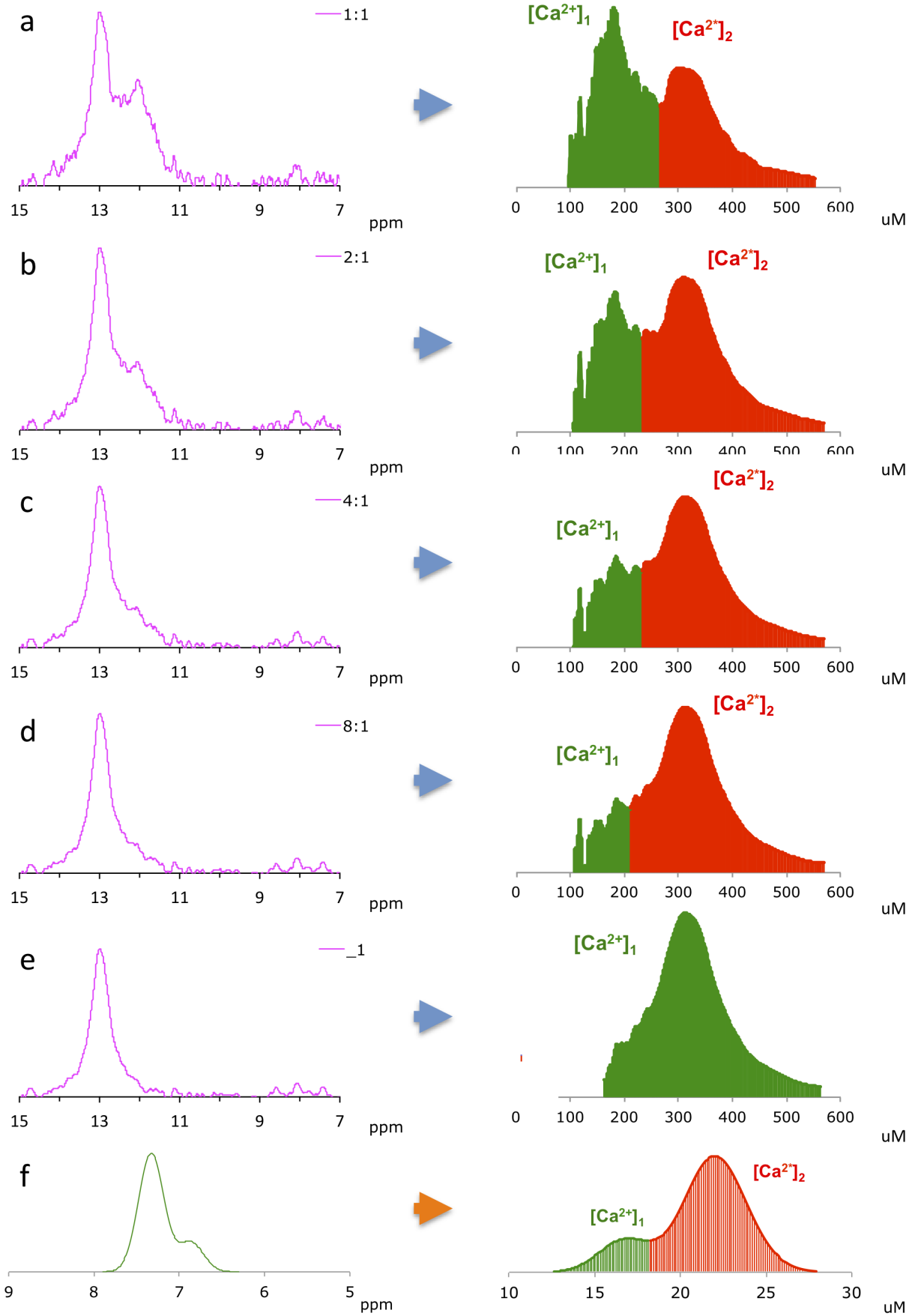
245

246 Owing to the high resolution of the underlying ^{19}F spectra, the resulting $[\text{Ca}^{2+}]_1$ and $[\text{Ca}^{2+}]_2$ modes are
247 perfectly invariant, which is not the case for low-field simulations (4.7 T, Table 1) that produce largely
248 overlapping $[\text{Ca}^{2+}]$ profiles (Fig. 1). As expected, the relatively narrow high-field spectral lines (in ppm)
249 resulted in smaller $[\text{Ca}^{2+}]$ standard deviations and ranges than the relatively broad low-field lines (Table 1).
250 As was to be anticipated, weighted $[\text{Ca}^{2+}]$ means and medians were closest for $[\text{Ca}^{2+}]$ distribution profiles
251 that deviated the least from a unimodal symmetric curve (for $i_1:i_2 = 0$ in Fig. 2, as well as for $i_1:i_2 = 0.125$
252 and 0.25, corresponding to ratios 1:8 and 1:4 in Table 1). While kurtosis was near zero for the unimodal
253 $[\text{Ca}^{2+}]$ profile ($i_1:i_2 = 0$), decreasing values with increasing $i_1:i_2$ accurately reflect the progressive
254 replacement of one dominating peak by two peaks (Fig. 2). Furthermore, the transition from a left-skewed
255 to a right-skewed profile from $i_1:i_2 = 0.125$ to $i_1:i_2 = 1.0$ is truthfully represented by increasing skewness
256 values. Another expected feature of our bimodal curves is that both area ratios ($a_1:a_2$) and peak height
257 ratios ($h_1:h_2$) increase nearly proportionally with $i_1:i_2$. In summary, statistical descriptors of $[\text{Ca}^{2+}]$
258 distributions calculated by our algorithms for a series of *in-silico* 4-FBAPTA ^{19}F MRS models,
259 straightforwardly reflect the behavior of the underlying $[\text{Ca}^{2+}]$ heterogeneity. Analogous data for 4-
260 FBAPTA ^{19}F spectra based on Lorentzians are presented in Supplementary Information, including Figure
261 S1 and Table S1 (S1 Supplemental Materials).

262 In practice, ^{19}F MRS line shapes underlying $[\text{Ca}^{2+}]$ distribution curves are not only influenced by Ca^{2+}
263 effects on chemical shift, but also by spurious effects, e.g., T_2 , T_2^* etc., as outlined in the Theory section
264 above. Assuming that the *individual* resonances making up the spectra plotted in Figure 1 are entirely
265 defined by such spurious effects, each bimodal $[\text{Ca}^{2+}]$ distribution shown is represented by two discrete
266 $[\text{Ca}^{2+}]$ values, *i.e.*, two Dirac δ functions (black vertical lines in second row of Fig. 1). Visual inspection
267 of this figure then suggests that for 4-FBAPTA, two modes, here equivalent to two distinct $[\text{Ca}^{2+}]$ values

268 differing by 1.0 μM ($[\text{Ca}^{2+}]_1$ and $[\text{Ca}^{2+}]_2$), can be clearly discerned at 7.0 T for all spectral amplitude ratios
269 from 1:1 to 1:8, but are unambiguously identified at 4.7 T only for ratios 1:1 and 1:2. For other ratios,
270 $[\text{Ca}^{2+}]$ differences were largely submerged by spurious line broadening. This indicates that $[\text{Ca}^{2+}]$ profiles
271 become more and more dominated by spurious effects as $[\text{Ca}^{2+}]$ differences decrease below 1.0 μM at 4.7
272 T, and below several 100 nM at 7.0 T. Consequently, the statistical descriptors presented in Figure 2 and
273 Table 1 should be seen as "effective" or "apparent" descriptors in the presence of major spurious effects
274 because they are greatly affected by factors other than $[\text{Ca}^{2+}]$ distribution (see also discussion below in
275 subsection 4.2). If obtained under these conditions, Table 1 shows that (apparent) statistical $[\text{Ca}^{2+}]$
276 distribution descriptors relating to curve shape (skewness, kurtosis, standard and normalized entropy) are
277 much less influenced by changes in amplitude ratios for 4.7 T vs. 7.0 T, in analogy to the case described
278 above for "pure" $[\text{Ca}^{2+}]$ distribution descriptors.

279



281 **Figure 3.** a - e: Left column: sums of two partially overlapping ^{19}F MRS resonances (two 5F/5'F peaks
282 from BAPTA-FF), measured at 376 MHz for model solutions containing 180 and 308 μM free Ca^{2+} .
283 Spectra were added as to yield amplitude ratios between from 1:1 to
284 8:1; one single resonance is also shown. Right column: $[\text{Ca}^{2+}]$ profiles obtained from corresponding
285 spectra on the right. Areas that can be associated with distinct modes are color-coded. Two modes ($[\text{Ca}^{2+}]_1$
286 and $[\text{Ca}^{2+}]_2$) differing by 128 μM can be clearly discerned for spectral amplitude ratios from 1:1 to 4:1.
287 However, broad lines (e.g., 210 Hz linewidth for the left peak after 20-Hz apodization for improved
288 signal-to-noise ratio, SNR) indicate that $[\text{Ca}^{2+}]$ distribution profiles are substantially influenced by
289 spurious effects. f: Envelope (sum) of two simulated Gaussian BAPTA-FF ^{19}F MRS resonances with 170
290 Hz linewidth (amplitude ratio 1:4, left), and the $[\text{Ca}^{2+}]$ profile derived from this envelope (right). The
291 centers of the individual Gaussians underlying each envelope were chosen such that the difference
292 between the $[\text{Ca}^{2+}]_1$ and $[\text{Ca}^{2+}]_2$ modes was about 5 μM .

293

294

295 **3.3. Measured profiles of $[\text{Ca}^{2+}]$ heterogeneity.** BAPTA-FF solutions have been prepared to model a
296 bimodal $[\text{Ca}^{2+}]$ distribution, with modes being centered at 0.18 and 0.31 mM. Since the K_d^{CaBAP} value for
297 BAPTA-FF is much higher (65 μM) than for 4-FBAPTA (2.9 μM), the optimally measurable $[\text{Ca}^{2+}]$ range
298 is increased by one to two orders of magnitude compared to 4-FBAPTA, as pointed out in the Theory
299 section. Our phantom $[\text{Ca}^{2+}]$ concentrations were chosen as to be within the range characteristic of real-
300 world tissue exhibiting elevated $[\text{Ca}^{2+}]_i$ values. For instance, Ca^{2+} concentration attributed to
301 heterogeneous sarcoplasmic reticulum populations in perfused rabbit heart has been shown to decrease
302 from about 1.5 to 0.3 mM [11], and even further down to < 0.1 mM [21] upon perfusion with a Ca^{2+} -
303 ATPase inhibitor. Thus, our BAPTA-FF solutions prepared to model unimodal and bimodal $[\text{Ca}^{2+}]$
304 distributions (0.18 and 0.31 mM Ca^{2+}) were within the $[\text{Ca}^{2+}]$ range given in these references [11,21].

305 Moreover, the $[\text{Ca}^{2+}]$ -sensitive 5F/5'F resonance of this compound is also more broadened by spurious
306 effects (essentially due to fast-to-intermediate exchange with $[\text{Ca}^{2+}]$). Figure 3 'a' to 'e' shows plots of the
307 two partially overlapping resonances at different intensity ratios and after 20-Hz apodization (left column),

308 akin to the bimodal resonances simulated for 4-FBAPTA (preceding subsections). The corresponding
309 calculated apparent $[Ca^{2+}]$ distributions were obtained after deconvolution with a Gaussian of 20 Hz
310 linewidth (right column). This deconvolution only partially took into account the exchange broadening of
311 the MRS resonance, which explains the rather broad lines even after deconvolution. Consequently, the
312 appearance of the resulting curves is far from the combinations of two Dirac δ functions theoretically
313 expected for a combination of two solutions each of which is characterized by one discrete Ca^{2+}
314 concentration. Nonetheless, the numerical results obtained for the statistical descriptors exhibited the
315 expected trends (Table 2, top), similar to those obtained for 4-FBAPTA-based simulations. With increasing
316 weight of the high-concentration mode (*i.e.*, from 'a' to 'd' in Fig. 3 and Table 2, top; see also Fig. 4), mean
317 and median $[Ca^{2+}]$ increased as the high-concentration (right) component increasingly dominated the
318 $[Ca^{2+}]$ profile. The latter feature also explains that both peak height and integrated peak area ratios (' $h_1:h_2$ '
319 and ' $a_1:a_2$ ') decreased, and skewness increased. The increasing peakedness of the distribution is reflected in
320 increasing kurtosis values, but standard and normalized entropy showed little variation (slight decrease).
321 Numerical values for the same BAPTA-FF resonance transformed upon 40 Hz apodization are given in
322 Table 2, bottom (see Fig. S2 for spectra and corresponding $[Ca^{2+}]$ profiles). While the general trends were
323 identical for 20-Hz and 40-Hz apodizations, the broader lines (for 40 Hz) necessarily caused increased
324 nominal values for standard deviation and range for peaks with roughly equal intensities ('a' and 'b'). The
325 increased overlap due to increased linewidth is reflected in altered ' $h_1:h_2$ ' and integrated ' $a_1:a_2$ ' values.
326 These differences, as well as increased skewness and kurtosis values, are also particularly pronounced for
327 the curves based on peaks with roughly equal intensities. Overall, the descriptors of the broader profiles
328 (40 Hz apodization) are less sensitive to changes in relative intensities of the low- and high-concentration
329 components than the narrower profiles (20 Hz apodization).

330

331 **Table 2.** Statistical descriptors for $[Ca^{2+}]$ curves based on experimental models of ^{19}F MR resonances of
332 BAPTA-FF, and for a $[Ca^{2+}]$ curve based on two simulated Gaussians

333

descriptors for 20 Hz LB	1:1 ^a	1:2 ^b	1:4 ^c	1:8 ^d	_1 ^e	simul. ^f
weighted mean (μM)	0.26	0.29	0.32	0.32	0.32	0.021
weighted median (μM)	0.24	0.28	0.30	0.31	0.31	0.022
std. deviation (μM)	0.10	0.11	0.12	0.12	0.08	0.003
range (μM)	0.47	0.56	0.71	0.71	0.40	0.017
mode, mg_1 (μM)	0.18	0.19	0.19	0.19	0.31	0.017
mode, mg_2 (μM)	0.31	0.31	0.31	0.31	-	0.022
global max. (μM)	0.18	0.31	0.31	0.31	0.31	0.022
peak height ratio ($h_1:h_2$)	1.51	0.83	0.60	0.45	-	0.29
peak area ratio integ. ($a_1:a_2$)	1.15	0.51	0.35	0.19	-	0.20
skewness, G1	0.587	0.725	1.156	1.175	0.479	-0.563
kurtosis, G2	-0.235	0.579	2.229	2.407	0.201	-0.100
stand. entropy, H_s	5.88	5.79	5.72	5.61	5.08	4.52
norm. entropy, H_n	0.61	0.60	0.59	0.58	0.57	0.62

334

335

336

337

338

339

340

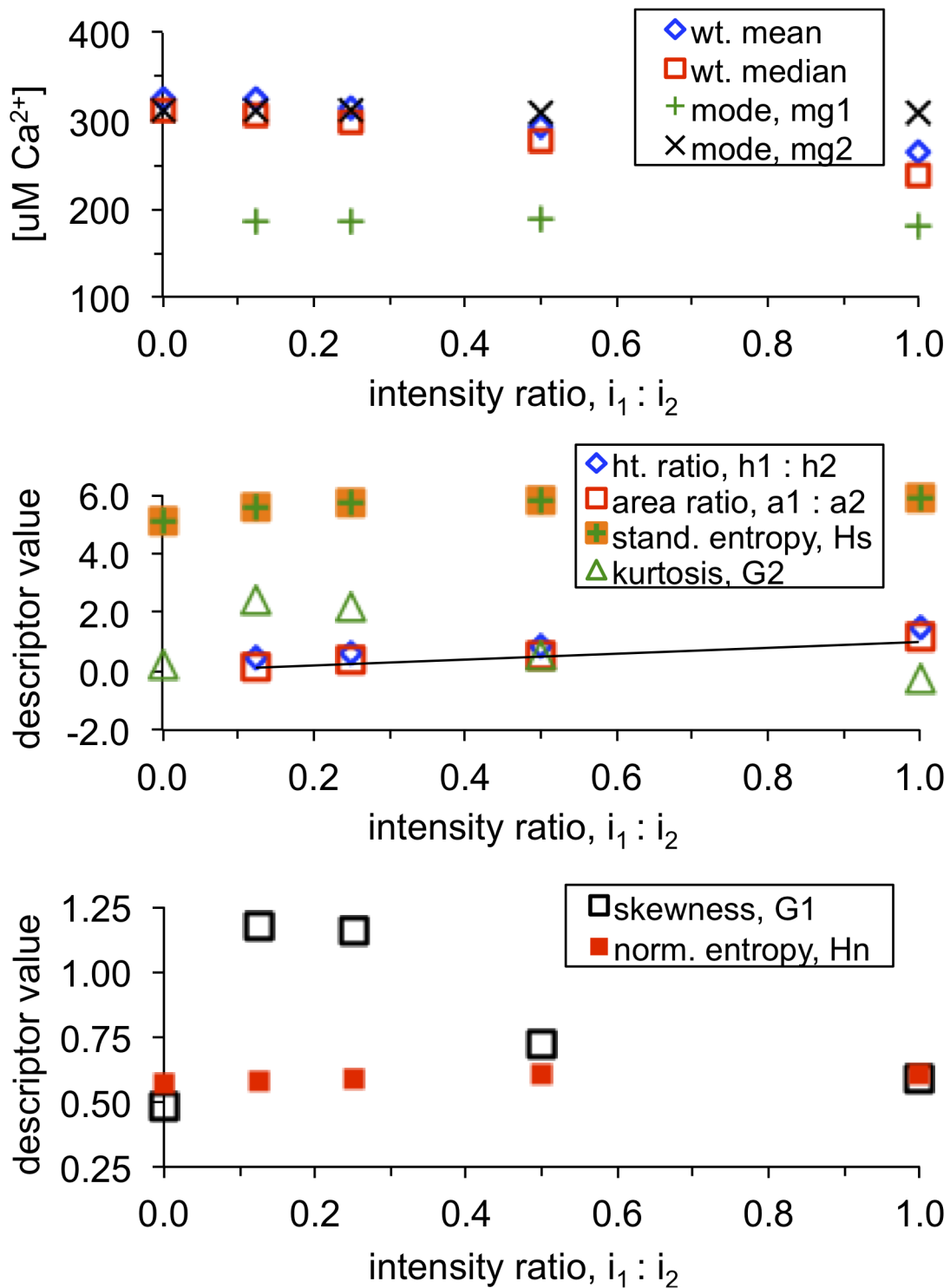
341

342

descriptors for 40 Hz LB	1:1 ^{a'}	1:2 ^{b'}	1:4 ^{c'}	1:8 ^{d'}	_1 ^{e'}
--------------------------	-------------------	-------------------	-------------------	-------------------	------------------

weighted mean (μM)	0.27	0.30	0.31	0.33	0.32
weighted median (μM)	0.25	0.28	0.30	0.31	0.31
std. deviation (μM)	0.11	0.12	0.11	0.12	0.08
range (μM)	0.53	0.63	0.63	0.69	0.40
mode, mg_1 (μM)	0.18	0.18	0.18	0.19	0.31
mode, mg_2 (μM)	0.31	0.31	0.31	0.31	-
global max. (μM)	0.18	0.31	0.31	0.31	0.31
peak height ratio ($h_1:h_2$)	1.34	0.84	0.57	0.43	-
peak area ratio integ. ($a_1:a_2$)	1.06	0.47	0.24	0.16	-
skewness, G1	0.752	0.951	0.908	1.281	0.481
kurtosis, G2	0.300	1.313	1.435	2.626	0.200
stand. entropy, H_s	5.92	5.81	5.68	5.52	5.08
norm. entropy, H_n	0.61	0.60	0.59	0.58	0.57

343 Indices a - f, top, refer to diagrams shown in Fig. 3. Indices a - e, bottom, refer to diagrams shown in Fig. S2.



344 **Figure 4.** Statistical descriptors for the [Ca²⁺] profiles presented in Figure 3. The straight line in
 345 the center panel shows that mode area ratios, $a_1:a_2$, are proportional to intensity ratios, $i_1:i_2$. Note that the
 346 units of the parameters shown in the middle and bottom panels are dimensionless.

347

348 As expected, the apparent $[Ca^{2+}]$ profile based on a single high-concentration 5F/5'F resonance from
349 BAPTA-FF ('e' in Fig. 3 and Table 2, top) yielded the same mean, median and mode values as the
350 envelope profile with the most dominating high-concentration component ('d'), but range and standard
351 deviations were much smaller for the single-peak profile. Another consequence of the derivation from a
352 single resonance is the finding of very small skewness and kurtosis values for 'e' (which are zero for pure
353 Gaussians). By contrast, the trend toward moderate decrease of standard and normalized entropy from 'a'
354 to 'd' is continued to 'e', reflecting the progressive transition from bimodal to unimodal behavior from 'a' to
355 'e'.

356 For comparison, a $[Ca^{2+}]$ distribution function, 'f', based on simulated 5F/5'F resonances of BAPTA-FF,
357 comparable to one of the experimental BAPTA-FF-derived curves (Fig. 3 c and Table 2 c, top), has been
358 evaluated for a lower Ca^{2+} concentration range. Direct quantitative comparisons of descriptor values
359 between measured and simulated distributions are not meaningful in view of the broad and noisy
360 experimental lines whose shapes are very different from Gaussians or Lorentzians. The simulated apparent
361 $[Ca^{2+}]$ profile nevertheless shows the expected negative skewness values because it is left-skewed, as
362 opposed to the experimental profiles with pronounced right tails. Kurtosis is close to zero because the
363 overall shape is dominated by the Gaussian of the high-concentration component, and slightly negative
364 due to the bulging flank caused by the low-concentration component. Standard and normalized entropy
365 values for the simulated $[Ca^{2+}]$ profile are of the same order of magnitude as those obtained for the
366 experimental profiles, as these descriptors do not depend on absolute concentration values or symmetry. In
367 summary, both measured and simulated $[Ca^{2+}]$ heterogeneity profiles based on BAPTA-FF ^{19}F spectra
368 yielded statistical $[Ca^{2+}]$ descriptors that are consistent with the respective lineshape characteristics.
369 Experimental $[Ca^{2+}]$ profiles indicated a very large influence of spurious effects on MRS lineshapes, in
370 agreement with previously published BAPTA-FF ^{19}F spectra from homogeneous solutions; these spectra
371 have been shown to exhibit broad and $[Ca^{2+}]$ -dependent linewidths for the 5F/5'F peak.

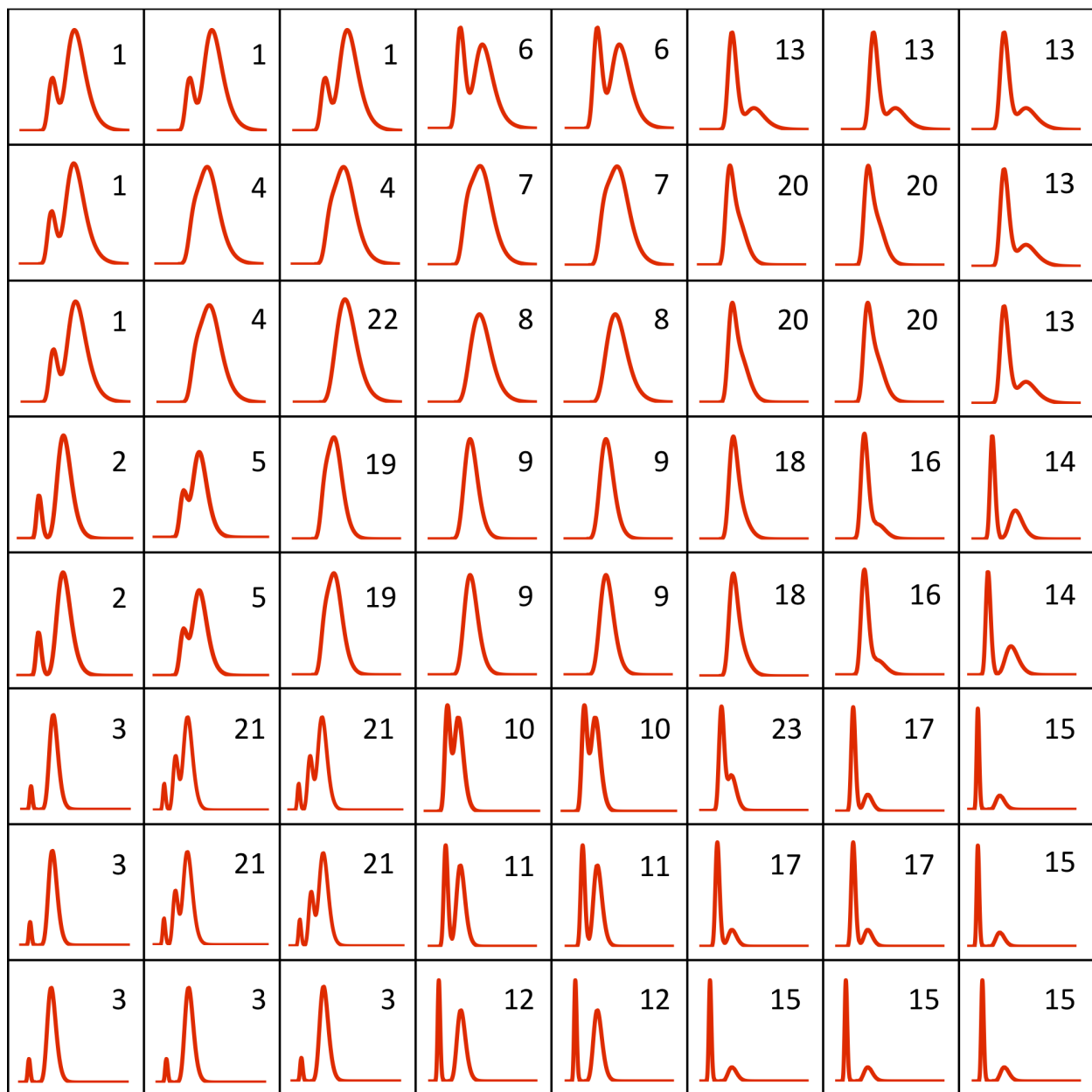
372

373 **3.4. Quantitative [Ca²⁺] heterogeneity analysis with ¹⁹F CSI - evaluation of numerical simulations.**

374 Next, we demonstrated the feasibility of combining statistical [Ca²⁺] information with spatial resolution
375 by simulating statistical CSI maps. These numerical simulations serve to demonstrate the proof of
376 principle for statistical [Ca²⁺] distribution maps based on ¹⁹F 4F-BAPTA MRSI, with the underlying [Ca²⁺]
377 profiles being evaluated with our algorithms presented above; they are not intended to mimic any
378 particular biological tissue. This goal was achieved by (i) simulating 23 [Ca²⁺] distribution profiles with
379 varying but well-defined characteristics, and (ii) assigning these profiles to 8x8 cells of a grid (Fig. 5)
380 underlying the 8x8 pixels of derived CSI maps, followed by interpolation (to 256x256 pixels) as is general
381 practice in CSI maps (Fig. 6). In addition, we simulated a "morphological" high-resolution (256x256) MR
382 image as a reference for localization (arbitrary pattern, Fig. S3).

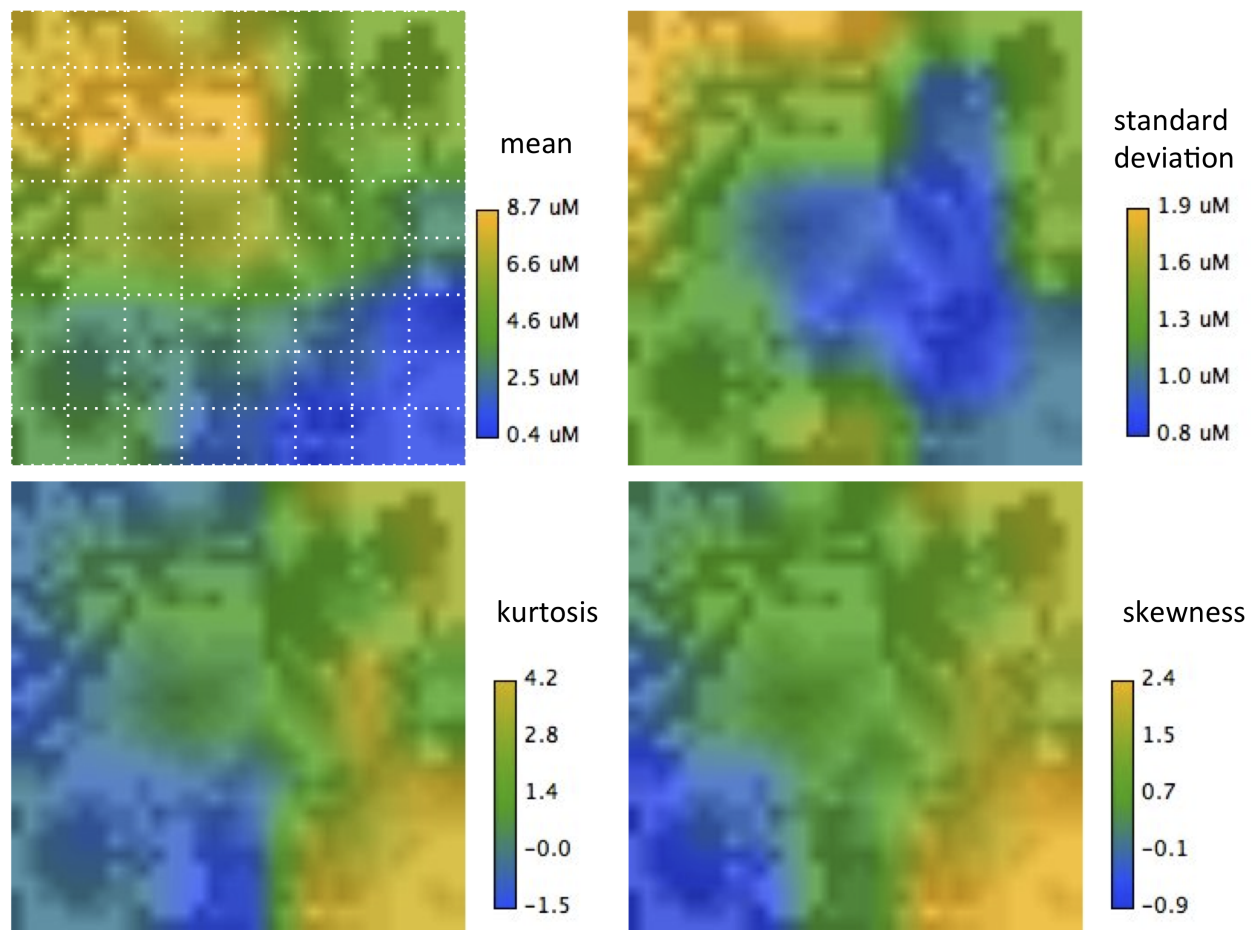
383 The rationale behind the construction of our exemplary [Ca²⁺] profiles and their distribution over the
384 grid was to create readily verifiable patterns as follows: in each CSI map (i) the simulated high-
385 concentration peak should increase from 4.5 to 7.5 μM (bottom to top); (ii) the overall distribution should
386 change from left-skewed to right-skewed (from left to right); and (iii) the distance between the low and
387 high-concentration modes underlying individual distributions should increase from the center to the edge
388 of the CSI maps. All profiles were created based on two more or less overlapping spectral lines, except for
389 trimodal profiles in subregions of the bottom left and top right quadrant of the CSI map (profiles 21 and
390 22; intermediate-concentration mode inserted between low and high-concentration modes). Note that in
391 several distributions, the bimodal or trimodal character is concealed by significant mode overlap. For these
392 CSI pixels, relative heights and areas of underlying modes were unavailable (white areas in Fig. S5,
393 bottom panels).

394 The statistical descriptors for each $[Ca^{2+}]$ distribution was calculated, and one CSI map for each obtained
395 descriptor was created (Figs. 6, S4 and S5). All panels of these figures exhibit color-coded CSI maps
396 representing different $[Ca^{2+}]$ distribution descriptors, each overlaid on a "morphological" image, as is
397 common for CSI presentations. Figure 6, top left panel, indicates the "true" spatial resolution of the CSI
398 maps (8x8 pixels, broken lines). Tables S2 - S4 contain the descriptor values for all $[Ca^{2+}]$ distributions
399 used, according to the numbering shown in Figure 5. The same descriptor values were also arranged in
400 spreadsheets as to directly represent all 8x8 CSI maps (EXCEL file "CSI maps pixel values.xlsx", S2
401 Supplemental Materials).



403 **Figure 5.** $[Ca^{2+}]$ distribution profiles, based on simulated 4-FBAPTA ^{19}F MR spectra, arranged in a 8x8
 404 matrix for the calculation of CSI maps shown in Figs. 6, S4 and S5. Simulations were purposefully
 405 designed such that (i) the simulated high-concentration peak increased from 4.5 to 7.5 μM , from bottom
 406 to top; (ii) the overall distribution changed from left-skewed to right-skewed, from left to right; and (iii)
 407 the distance between the low and high-concentration modes underlying the overall distributions increased

408 from the center to the edge of the matrix. The statistical $[Ca^{2+}]$ distribution descriptors for spectra
409 numbered 1 to 23 are presented in Tables S2 - S4.
410



412 **Figure 6.** Color-coded CSI maps for mean, standard deviation, kurtosis and skewness of the $[Ca^{2+}]$
413 distribution profiles shown in Figure 5. The top left CSI map indicates the real spatial resolution based on
414 an 8x8 matrix (broken lines), before interpolation to 256x256 pixels. The black-and-white background
415 structure in each CSI map has been generated by simulation; see reference image in Fig. S3.

416

417 The CSI maps clearly reflect the statistical properties of the CSI pixels. In Fig. 6, lowest mean $[Ca^{2+}]$
418 values are seen in the bottom right corner of the relevant CSI map ("mean"), representing the distributions
419 with the most intense low-concentration mode; and highest values are present near the top left corner
420 where a rather broad high-concentration mode dominates the distribution (Fig. 5). Standard deviations
421 were highest in the top left corner of the pertinent map because of the particularly broad overall
422 distribution, whereas $[Ca^{2+}]$ values are concentrated within a small range for CSI pixels at and close to the
423 right of the center (Fig. 5). Highest kurtosis values were generally found in the right half of the kurtosis
424 map, with a prevalence of profiles dominated by narrow single peaks. By contrast, the presence of
425 multiple and/or broad peaks lead to low kurtosis values. The transition from left to right skew is best seen
426 in the bottom half of the skewness map, whereas the broadening of the distributions at the top of the map
427 tended to wash out any major left or right skew (predominantly slight right skew; Fig. 5).

428

429

430 **4. Discussion**

431 **4.1. Proof of principle.** The proof of principle for the first method enabling quantitative characterization
432 of heterogeneity in Ca^{2+} concentration was provided in a basic feasibility study. The underlying paradigms
433 and algorithms were presented and validated for ^{19}F MRS of two Ca^{2+} reporter molecules, 4-FBAPTA and
434 BAPTA-FF. Calculated statistical descriptors of $[Ca^{2+}]$ distribution profiles were evaluated based on *in*
435 *silico* and experimental *in vitro* approaches, for different magnetic field strengths and $[Ca^{2+}]$ distribution
436 models. Thus, the fundamental suitability of this method for the determination of quantitative parameters
437 describing the statistical distribution of intracellular $[Ca^{2+}]$ has been established.

438

439 **4.2. The influence of spurious effects.** Current limitations of our novel technique are due to spurious
440 effects on $[Ca^{2+}]$ distribution profiles, *i.e.*, effects that are unrelated to chemical-shift effects of $[Ca^{2+}]$ on
441 the Ca^{2+} -sensitive ^{19}F resonance of the reporter molecule in question. Spurious effects may broaden ^{19}F
442 resonances principally due to T_2 and T_2^* mechanisms and ^{19}F - 1H J coupling, and may thus lead to $[Ca^{2+}]$
443 profile shapes that no longer truthfully reflect the underlying $[Ca^{2+}]$ distribution. There are several ways of
444 dealing with spurious effects. Prior to signal acquisition, the shim on the very volume to be used for ^{19}F
445 MRS should be optimized. Modern MR systems provide shim sequences that automatically adjust the
446 shim gradients such that the field is optimally homogenized for a user-defined volume. This procedure can
447 minimize line shape distortions due to magnetic field inhomogeneity. Despite these precautions, resulting
448 line shapes will still be affected by spurious effects. Therefore, experimentally observed line shapes
449 represent a combination of $[Ca^{2+}]$ heterogeneity and spurious effects, although the latter can be largely
450 compensated for by the reference deconvolution technique mentioned above and in the following
451 subsection, and first introduced and discussed in much more detail in previous papers [17,19,20] (see also
452 S1 Supplemental Materials). However, even the apparent descriptor values obtainable without reference
453 deconvolution (subsection 3.2) are useful if they are employed as relative (as opposed to absolute) values.
454 For instance, differences in apparent descriptor values for a particular group of experimental animals *vs.*
455 those obtained for a control group provide information on the difference in $[Ca^{2+}]$ heterogeneity between
456 these groups. Of course, in this case all individual measurements involved should be performed under
457 identical experimental conditions.

458 Our validation results closely parallel previously obtained findings for $[Mg^{2+}]$ distributions (obtained
459 from analogous simulated ATP- β ^{31}P MR spectra) that had also been studied for reference-deconvolved
460 spectra [17]. Therefore, it was not necessary to repeat the $[Ca^{2+}]$ distribution analysis of subsection 3.2. for
461 the corresponding deconvolved spectra; instead, we simply point here to the results contained in that
462 previous report [17] indicating increased sensitivity to differences in metal ion concentration upon
463 deconvolution. In future *in-vivo* applications, reference functions to be applied in deconvolution will be

464 empirical, *i.e.*, they will involve the corresponding experimentally measured Ca^{2+} -sensitive F-BAPTA
465 resonances from appropriate biological tissues with homogeneous $[\text{Ca}^{2+}]$, in analogy with the previously
466 described application of ^{31}P MRS to ATP- β . This will lead to significantly decreased values for evaluable
467 $[\text{Ca}^{2+}]$ differences, again in analogy with results previously obtained in $[\text{Mg}^{2+}]$ distribution analysis [17].
468 Moreover, ongoing developments geared toward $[\text{Ca}^{2+}]$ -dependent deconvolution functions should further
469 increase the sensitivity of our method to small $[\text{Ca}^{2+}]$ differences, as they will take into account F-BAPTA
470 linewidth variations with $[\text{Ca}^{2+}]$ due to varying F-BAPTA/ Ca^{2+} exchange rates.

471

472 **4.3. Sensitivity of F-BAPTA ^{19}F MRS and MRSI.** Conventional $[\text{Ca}^{2+}]$ analysis by ^{19}F MRS of BAPTA-
473 FF in biological tissues has demonstrated that a high-quality 1D spectrum can be acquired over a period of
474 5 minutes for a single-volume acquisition, yielding a SNR of about 10 [10,11]. This is also the SNR we
475 consider to be the minimum for our new evaluation strategy. Note that no matter how low the Ca^{2+}
476 concentration, we always measure the full intensity of the BAPTA ^{19}F MR signal. This is due to the fact
477 that variations in Ca^{2+} concentration under conditions of fast exchange (on the NMR scale) between Ca^{2+}
478 and the fluorinated BAPTA compound only change the chemical shift of the $[\text{Ca}^{2+}]$ -sensitive ^{19}F -BAPTA
479 peak, but not its intensity. Thus, it is only the fluorinated BAPTA concentration that determines sensitivity
480 in terms of SNR, not the Ca^{2+} concentration of the sample. The feasibility of *F-BAPTA* MRS in terms of
481 SNR has also been confirmed for actual in vivo and in situ measurements with a related F-BAPTA
482 compound [13], as mentioned in the Introduction section. In all cases, tissue concentrations of the Ca^{2+}
483 reporter molecules in question typically are in the millimolar range [10,11], *i.e.*, in the same concentration
484 range as many metabolites that are comfortably measured by in vivo ^1H monovoxel MRS and MRSI (CSI)
485 methods. Note that the ^{19}F nucleus (i) is only slightly less NMR sensitive than ^1H , (ii) occurs at 100%
486 natural abundance, and (iii) has the added advantage of no background signal when compared to ^1H MRS
487 and MRSI, As was to be expected on the basis of these considerations, the practical feasibility of in vivo

488 ^{19}F MRSI has been repeatedly demonstrated for fluorinated drug metabolites [25–27], but also for gene-
489 reporter molecules [28]. Owing to the absence of particular sensitivity issues, ^{19}F MRSI would also be
490 feasible for BAPTA-FF, 4-FBAPTA and other Ca^{2+} -sensitive fluorinated chelates. In these cases, one ^{19}F
491 spectrum would be obtained for each CSI voxel. However, simply converting "the" chemical shift of each
492 Ca^{2+} -sensitive F-BAPTA line to a $[\text{Ca}^{2+}]$ value would lead to a $[\text{Ca}^{2+}]$ map that ignores any intravoxel
493 $[\text{Ca}^{2+}]$ heterogeneity, and may not even represent an accurate average $[\text{Ca}^{2+}]$ value for each resolved voxel,
494 depending on the shape of the underlying statistical $[\text{Ca}^{2+}]$ profile. This is in direct analogy to the situation
495 described above for 1D ^{19}F MR spectra. Combining our new method for evaluating statistical $[\text{Ca}^{2+}]$
496 profiles with the spatial resolution of CSI would be a way of adding information on statistical $[\text{Ca}^{2+}]$
497 distribution to spatial information. Nonetheless, spatial resolution based on MRSI will remain somewhat
498 limited by sensitivity, even if relatively fast CSI variants such as EPSI are used. Therefore, whenever fast
499 Ca^{2+} imaging at high spatial resolution is desired, appropriate methods based on CEST/F-BAPTA or smart
500 T_1 relaxation agents should be used, to the extent that these recently developed methods turn out to be
501 reliable in vivo. In such cases, our current new spectroscopic approach would provide complementary
502 multiparametric statistical information on total $[\text{Ca}^{2+}]$ distribution that is not available through these new
503 Ca^{2+} imaging methods.

504 Sensitivity of our $[\text{Ca}^{2+}]$ distribution curves to *differences* in $[\text{Ca}^{2+}]$ within a heterogeneous sample is a
505 separate issue; the latter is totally unrelated to the SNR issue discussed in the preceding paragraph and has
506 been thoroughly analyzed in the Results section for two different chelators (BAPTA-FF and 4F-BAPTA),
507 for characteristic $[\text{Ca}^{2+}]$ ranges. A given variation in $[\text{Ca}^{2+}]$ has a relatively large effect on the chemical
508 shift of the ^{19}F -BAPTA signal if the actual $[\text{Ca}^{2+}]$ values to be analyzed are close to the K_d value of the
509 Ca^{2+} /F-BAPTA complex, because changes in $[\text{Ca}^{2+}]$ close to K_d have large effects on the ratio of free vs.
510 complexed chelator concentrations. This leads to $[\text{Ca}^{2+}]$ distribution curves and associated statistical
511 descriptors finely mirroring even relatively small $[\text{Ca}^{2+}]$ differences. In other words, the " $[\text{Ca}^{2+}]$ resolution"
512 is relatively high. By contrast, if the actual $[\text{Ca}^{2+}]$ values are much lower or much higher than K_d , $[\text{Ca}^{2+}]$

513 variations have very little effect on the ratio of free vs. complexed chelator concentrations because nearly
514 all BAPTA species are free or complexed, respectively. In this case, effects of $[Ca^{2+}]$ variations on
515 chemical shift are very small and hardly discernable in derived $[Ca^{2+}]$ distribution curves and associated
516 statistical descriptors as small $[Ca^{2+}]$ variations are averaged out. As a consequence, the "[Ca^{2+}] resolution"
517 is relatively low. Accordingly, for our method to be powerful, the fluorinated $[Ca^{2+}]$ chelator should be
518 chosen such that the order of magnitude of its K_d is approximately that of the actual $[Ca^{2+}]$ values of
519 interest. Conversely, a given $[Ca^{2+}]$ chelator should only be used to study $[Ca^{2+}]$ values that are
520 approximately on the order of magnitude of the K_d value of that chelator. These requirements are in strict
521 analogy with those for classical applications of ^{19}F -BAPTA MRS analysis of $[Ca^{2+}]$ where the K_d value
522 determines the $[Ca^{2+}]$ range for which Ca^{2+} concentrations can be measured with reasonable precision. As
523 explained above in the Theory section, London et al. [23] and Murphy et al. [10] have shown that the
524 relatively high K_d value of BAPTA-FF/ Ca^{2+} (65 μM) makes it ideal for measuring elevations in $[Ca^{2+}]_i$
525 occurring, e.g., in heart during ischemia (values $> 2 \mu M$), but inappropriate for basal $[Ca^{2+}]_i$ values that are
526 much lower. By contrast, 4-FBAPTA used in our simulations has a much lower K_d value with Ca^{2+} , and
527 would therefore be useful for measuring basal $[Ca^{2+}]_i$ levels ($\leq 1 \mu M$). In summary, it is neither our new
528 approach nor the classical ^{19}F -BAPTA MRS method *per se* that define the reasonable $[Ca^{2+}]$ range, but
529 only the K_d value of the fluorinated reporter molecule employed.

530

531

532 **4.4. Potential confounding parameters.** In the Theory section we have stated that actual K_d values for
533 F-BAPTA/ Ca^{2+} complexes in different biological tissues may vary slightly as a function of intracellular
534 parameters such as pH and ion concentration. In fact, the issue of potential interference by the most
535 relevant parameters, $[Mg^{2+}]$ and pH, with $[Ca^{2+}]$ analysis by ^{19}F MRS of BAPTA-FF has already been
536 studied by London et al. in the context of the classical application of this method, both theoretically and

537 experimentally [23]. Since our new approach was experimentally investigated using the same fluorinated
538 $[Ca^{2+}]$ chelator, we directly refer to their results in the following. As for pH, significant effects were only
539 found for rather acidic milieus, i.e., below pH 6.25 to 6.50 (Fig. 6 in [23]). For instance, from the upper
540 (alkaline) limit down to pH 7.1, the chemical shift of the 5,5'-F resonance only changed by a negligible 0.2
541 % of the difference between the shifts for pH values of fully protonated and fully deprotonated BAPTA-
542 FF. On the other hand, mammalian cells are not usually viable at intracellular pH values significantly
543 below 7.0; even transiently lowering intracellular pH to 6.5 or less causes necrosis, apoptosis, or both
544 forms of cell death. (We disregard cases where pH_i is diminished only for a fraction of a second; these
545 cases are irrelevant here because a typical $[Ca^{2+}]_i$ measurement by ^{19}F -BAPTA-FF MRS may take a few
546 minutes). It would be of little interest to try measuring "intracellular" $[Ca^{2+}]$ for cells that are
547 disintegrating, i.e., where intracellular and extracellular spaces are no longer defined in the first place. As
548 for $[Mg^{2+}]$, the authors found that millimolar changes could indeed lead to measurable errors in the $[Ca^{2+}]$
549 determination for $[Ca^{2+}]$ values near basal values of several hundred nanomolar. As mentioned in the
550 above, this order of magnitude for $[Ca^{2+}]$ is certainly too low to be measured by way of BAPTA-FF with
551 any acceptable degree of accuracy. However, for accessible $[Ca^{2+}]$ well above baseline levels (London et
552 al. mention heart tissue during ischemia), changes in $[Mg^{2+}]$ have a negligible effect on $[Ca^{2+}]$ values
553 measured by ^{19}F -BAPTA-FF MRS. As for 4F-BAPTA, Smith et al. have shown that the chemical shift of
554 its ^{19}F resonance is very insensitive to Mg^{2+} and pH, and that 4F-BAPTA therefore provides a direct
555 measurement of $[Ca^{2+}]$ without correction for Mg^{2+} and pH [5]. The same authors have demonstrated that
556 other ions (Zn^{2+} , Fe^{2+} , Mn^{2+} , etc.) are in slow exchange with 4F-BAPTA, and therefore will not affect the
557 4F-BAPTA/ Ca^{2+} resonance [5].

558 For these reasons, we can neglect both pH and $[Mg^{2+}]$ effects in the context of our current report.
559 However, further refinements such as optimization for particular tissue types should be envisaged in future
560 research projects. Such tissue-specific work would also include (i) considering tissues with particularly
561 high or low protein levels, and (ii) studying the influence of ^{19}F MR spectrum deconvolution on the

562 practical *in vivo* limitations of our method.

563

564 **4.5. Future developments.** Depending on the concentration range to be measured, spurious line
565 broadening may be particularly strong due to the influence of intermediate-to-fast exchange rates on T_2 .
566 Although advanced reference deconvolution procedures currently under development should be able to
567 tackle this issue by compensating $[Ca^{2+}]$ -dependent line width effects, a more straightforward, powerful
568 and elegant solution would be the use of fluorinated $[Ca^{2+}]$ chelators producing very fast exchange rates.
569 This would greatly simplify the deconvolution process. To the best of our knowledge, such chelators are
570 not currently available. Therefore, it would be strongly desirable to see such fluorinated compounds
571 developed in the future. Once available, these new compounds would render our new method even more
572 powerful by facilitating work at relatively high field strengths (9.4 or 11.7 T, and above). In addition to
573 exchange rates, attention must be paid to the dissociation constant, K_d , of the complex between Ca^{2+} and
574 the fluorinated chelator. As outlined above, some currently available compounds such as BAPTA-FF are
575 only useful when Ca^{2+} concentrations are involved that are one to two orders of magnitude above the basal
576 values typical of mammalian cells. Future efforts should be directed toward the development of a pool of
577 fast-exchanging fluorinated $[Ca^{2+}]$ chelators representing a range of K_d values, from which a particular
578 compound can be chosen as a function of the Ca^{2+} concentration of interest. Once confirmed by *in-vivo*
579 experiments, potential biomedical applications of our quantitative $[Ca^{2+}]$ heterogeneity measurements may
580 include a range of conditions affecting the concentration of free intracellular Ca^{2+} , notably in heart, muscle
581 and brain tissue. This approach should help clarify the nature and extent of pathological processes
582 involving major perturbations of $[Ca^{2+}]$ regulation.

583 The past few years have seen an impressive increase in publications applying "machine learning"
584 procedures to the analysis of results from biomedical investigations (see [29] and [30] for reviews). These
585 techniques include numerous data mining algorithms used for preprocessing, classification and clustering

586 as well as various optimized neural network architectures in "deep learning" methods. These advanced
587 routines can be thought of as higher-level statistics or "meta-statistics", and have been successfully used in
588 metabolomics and other omics sciences. In this context, the multiple statistical descriptors generated by
589 our new approach may be combined with further metabolic, biochemical, biological and imaging
590 parameters to characterize tissue in vivo by using neural network and other machine learning algorithms.
591 This deeper level of analysis should facilitate the discovery of complex patterns relevant to healthy and
592 diseased tissues that may be difficult or impossible to identify in the conventional way, i.e., by operators
593 not assisted by artificial intelligence.

594

595

596 **5. Methods**

597 A series of Tris base/HEPES-buffered BAPTA-FF solutions was prepared with varying Ca^{2+}
598 concentrations [23]. ^{19}F MR spectra were acquired at 376 MHz with a spectral width of 30 ppm, an FID
599 length of 8 k data points (0.364 s), and a total of 2048 transients. Spectra were apodized with 20 or 40 Hz
600 before Fourier transformation. After referencing to the 6,6'- ^{19}F resonance and baseline correction, spectra
601 were transferred to our EXCEL template (see S1 Supplemental Software). Subsequently, spectra were
602 either directly subjected to chemical shift-to- $[\text{Ca}^{2+}]$ conversion or processed with reference deconvolution
603 (described above) before conversion. Statistical analysis of the underlying distribution of $[\text{Ca}^{2+}]$ values
604 ensued, based on the equations given above and in S1 Supplemental Materials (the latter file also contains
605 further methodological details).

606

607

608 **6. References**

- 609 [1] M. Brini, D. Ottolini, T. Cali, E. Carafoli, Calcium in health and disease, *Met Ions Life Sci.* 13
610 (2013) 81–137. doi:10.1007/978-94-007-7500-8_4.
- 611 [2] C.H. Wilson, E.S. Ali, N. Scrimgeour, A.M. Martin, J. Hua, G.A. Tallis, G.Y. Rychkov, G.J.
612 Barritt, Steatosis inhibits liver cell store-operated Ca(2)(+) entry and reduces ER Ca(2)(+) through a
613 protein kinase C-dependent mechanism, *Biochem J.* 466 (2015) 379–90. doi:10.1042/BJ20140881.
- 614 [3] L. Annunziato, Sodium calcium exchange: a growing spectrum of pathophysiological
615 implications, Springer, New York, 2013.
- 616 [4] M. Peacock, Calcium metabolism in health and disease, *Clin J Am Soc Nephrol.* 5 Suppl 1 (2010)
617 S23-30. doi:10.2215/CJN.05910809.
- 618 [5] G.A. Smith, R.T. Hesketh, J.C. Metcalfe, J. Feeney, P.G. Morris, Intracellular calcium
619 measurements by ¹⁹F NMR of fluorine-labeled chelators, *Proc Natl Acad Sci U A.* 80 (1983) 7178–82.
- 620 [6] J.C. Metcalfe, T.R. Hesketh, G.A. Smith, Free cytosolic Ca²⁺ measurements with fluorine
621 labelled indicators using ¹⁹F NMR, *Cell Calcium.* 6 (1985) 183–95.
- 622 [7] E. Marban, M. Kitakaze, V.P. Chacko, M.M. Pike, Ca²⁺ transients in perfused hearts revealed by
623 gated ¹⁹F NMR spectroscopy., *Circ. Res.* 63 (1988) 673–678.
- 624 [8] E. Marban, M. Kitakaze, Y. Koretsune, D.T. Yue, V.P. Chacko, M.M. Pike, Quantification of
625 [Ca²⁺]_i in perfused hearts. Critical evaluation of the 5F-BAPTA and nuclear magnetic resonance method
626 as applied to the study of ischemia and reperfusion., *Circ. Res.* 66 (1990) 1255–1267.
- 627 [9] M.C. Corretti, Y. Koretsune, H. Kusuoka, V.P. Chacko, J.L. Zweier, E. Marban, Glycolytic
628 inhibition and calcium overload as consequences of exogenously generated free radicals in rabbit hearts.,
629 *J. Clin. Invest.* 88 (1991) 1014–1025. doi:10.1172/JCI115361.
- 630 [10] E. Murphy, C. Steenbergen, L.A. Levy, S. Gabel, R.E. London, Measurement of cytosolic free
631 calcium in perfused rat heart using TF-BAPTA., *Am. J. Physiol.* 266 (1994) C1323-1329.
632 doi:10.1152/ajpcell.1994.266.5.C1323.
- 633 [11] W. Chen, C. Steenbergen, L.A. Levy, J. Vance, R.E. London, E. Murphy, Measurement of free
634 Ca²⁺ in sarcoplasmic reticulum in perfused rabbit heart loaded with 1,2-bis(2-amino-5,6-
635 difluorophenoxy)ethane-N,N,N',N'-tetraacetic acid by ¹⁹F NMR., *J. Biol. Chem.* 271 (1996) 7398–7403.
- 636 [12] J. Chen, J. Petranka, K. Yamamura, R.E. London, C. Steenbergen, E. Murphy, Gender differences

637 in sarcoplasmic reticulum calcium loading after isoproterenol., *Am. J. Physiol. Heart Circ. Physiol.* 285
638 (2003) H2657-2662. doi:10.1152/ajpheart.00557.2003.

639 [13] S.K. Song, R.S. Hotchkiss, J. Neil, P.E.J. Morris, C.Y. Hsu, J.J. Ackerman, Determination of
640 intracellular calcium in vivo via fluorine-19 nuclear magnetic resonance spectroscopy., *Am. J. Physiol.*
641 269 (1995) C318-322. doi:10.1152/ajpcell.1995.269.2.C318.

642 [14] A. Bar-Shir, A.A. Gilad, K.W. Chan, G. Liu, P.C. van Zijl, J.W. Bulte, M.T. McMahon, Metal ion
643 sensing using ion chemical exchange saturation transfer 19F magnetic resonance imaging, *J Am Chem*
644 *Soc.* 135 (2013) 12164–7. doi:10.1021/ja403542g.

645 [15] A. Moussaron, S. Vibhute, A. Bianchi, S. Gunduz, S. Kotb, L. Sancey, V. Motto-Ros, S.
646 Rizzitelli, Y. Cremillieux, F. Lux, N.K. Logothetis, O. Tillement, G. Angelovski, Ultrasmall
647 Nanoplatfoms as Calcium-Responsive Contrast Agents for Magnetic Resonance Imaging., *Small Weinh.*
648 *Bergstr. Ger.* 11 (2015) 4900–4909. doi:10.1002/sml.201500312.

649 [16] K. Dhingra, P. Fouskova, G. Angelovski, M.E. Maier, N.K. Logothetis, E. Toth, Towards
650 extracellular Ca²⁺ sensing by MRI: synthesis and calcium-dependent 1H and 17O relaxation studies of
651 two novel bismacrocylic Gd³⁺ complexes., *J. Biol. Inorg. Chem. JBIC Publ. Soc. Biol. Inorg. Chem.* 13
652 (2008) 35–46. doi:10.1007/s00775-007-0296-9.

653 [17] N.W. Lutz, M. Bernard, Multiparametric quantification of heterogeneity of metal ion
654 concentrations, as demonstrated for [Mg²⁺] by way of 31P MRS, *J Magn Reson.* 294 (2018) 71–82.
655 doi:10.1016/j.jmr.2018.06.016.

656 [18] N.W. Lutz, Y. Le Fur, J. Chiche, J. Pouyssegur, P.J. Cozzone, Quantitative in-vivo
657 characterization of intracellular and extracellular pH profiles in heterogeneous tumors: a novel method
658 enabling multiparametric pH analysis, *Cancer Res.* 73 (2013) 4616–4628. doi:10.1158/0008-5472.CAN-
659 13-0767.

660 [19] N.W. Lutz, M. Bernard, Multiparametric quantification of thermal heterogeneity within aqueous
661 materials by water 1H NMR spectroscopy: paradigms and algorithms, *PLOS ONE.* 12 (2017) e0178431.

662 [20] N.W. Lutz, M. Bernard, Thermal heterogeneity within aqueous materials quantified by 1H NMR
663 spectroscopy: Multiparametric validation in silico and in vitro, *J. Magn. Reson.* 287 (2017) 56–64.

664 [21] S. Yanagida, C.S. Luo, J.A. Balschi, G.M. Pohost, M.M. Pike, Simultaneous multicompartent
665 intracellular Ca²⁺ measurements in the perfused heart using 19F NMR spectroscopy, *Magn Reson Med.*

- 666 35 (1996) 640–7.
- 667 [22] R.K. Gupta, P. Gupta, R.D. Moore, NMR studies of intracellular metal ions in intact cells and
668 tissues, *Annu. Rev. Biophys. Bioeng.* 13 (1984) 221–46.
- 669 [23] R.E. London, C.K. Rhee, E. Murphy, S. Gabel, L.A. Levy, NMR-sensitive fluorinated and
670 fluorescent intracellular calcium ion indicators with high dissociation constants, *Am J Physiol.* 266 (1994)
671 C1313-22.
- 672 [24] J. Hasenauer, S. Waldherr, M. Doszczak, N. Radde, P. Scheurich, F. Allgöwer, Identification of
673 models of heterogeneous cell populations from population snapshot data, *BMC Bioinformatics.* 12 (2011)
674 125. doi:10.1186/1471-2105-12-125.
- 675 [25] O. Gonen, J. Murphy-Boesch, C.W. Li, K. Padavic-Shaller, W.G. Negendank, T.R. Brown,
676 Simultaneous 3D NMR spectroscopy of proton-decoupled fluorine and phosphorus in human liver during
677 5-fluorouracil chemotherapy., *Magn. Reson. Med.* 37 (1997) 164–169.
- 678 [26] A.S. Dzik-Jurasz, D.J. Collins, M.O. Leach, I.J. Rowland, Gallbladder localization of (19)F MRS
679 catabolite signals in patients receiving bolus and protracted venous infusional 5-fluorouracil., *Magn.*
680 *Reson. Med.* 44 (2000) 516–520.
- 681 [27] D.W. Klomp, H.W. Van Laarhoven, A.P. Kentgens, A. Heerschap, Optimization of localized 19F
682 magnetic resonance spectroscopy for the detection of fluorinated drugs in the human liver, *Magn Reson*
683 *Med.* 50 (2003) 303–308.
- 684 [28] V.D. Kodibagkar, J. Yu, H.P. Hetherington, R.P. Mason, Imaging beta-galactosidase activity
685 using 19F chemical shift imaging of LacZ gene-reporter molecule 2-fluoro-4-nitrophenol-beta-D-
686 galactopyranoside, *Magn Reson Imaging.* 24 (2006) 959–962.
- 687 [29] K. Lan, D.-T. Wang, S. Fong, L.-S. Liu, K.K.L. Wong, N. Dey, A Survey of Data Mining and
688 Deep Learning in Bioinformatics., *J. Med. Syst.* 42 (2018) 139. doi:10.1007/s10916-018-1003-9.
- 689 [30] D.M. Camacho, K.M. Collins, R.K. Powers, J.C. Costello, J.J. Collins, Next-Generation Machine
690 Learning for Biological Networks., *Cell.* 173 (2018) 1581–1592. doi:10.1016/j.cell.2018.05.015.

691

692 **Supporting Information**

693 **S1 Supplemental Materials.** Further Algorithms, Validations; Figures S-1 through S-5, Tables S1
694 through S4.

695 (PDF)

696

697 **S2 Supplemental Materials.** Pixel values of CSI maps.

698 (XLSX)

699

700 **S1 Supplemental Software.** Template spreadsheet with calculation example for statistical descriptors of
701 $[\text{Ca}^{2+}]$ heterogeneity.

702 (XLSX)

703